Journal of Materials Chemistry A

ROYAL SOCIETY OF CHEMISTRY

PAPER

View Article Online
View Journal

Cite this: DOI: 10.1039/d5ta05965h

Silver single atom in polymeric carbon nitride as a stable and selective oxygen reduction electrocatalyst towards hydrogen peroxide synthesis

Akanksha Gupta,†[a] Manoj Shanmugasundaram,†[ab] Shilendra Kumar Sharma,[c] Sudip Chakraborty[c] and David Zitoun*[ab]

Electrochemical hydrogen peroxide (H_2O_2) synthesis *via* the two-electron oxygen reduction reaction ($2e^-$ ORR) offers a promising alternative to the traditional anthraquinone process. In this study, we report a silver single-atom catalyst Ag(I) coordinated within a polymeric carbon nitride (PCN) framework (Ag–PCN), as a highly selective and durable electrocatalyst for H_2O_2 generation. For the first time, particular attention was given to evaluating catalyst stability under harsh oxidative conditions, specifically 3% H_2O_2 solution for one week. Ag–PCN exhibited superior H_2O_2 selectivity in 0.1 M $KHCO_3$ compared to pristine PCN. Although pristine PCN initially showed higher activity, it suffered from poor oxidative stability, losing 9% of its mass, whereas Ag–PCN displayed only 1% of mass loss. Inductively coupled plasma (ICP) analysis further confirmed minimal Ag leaching (0.3 wt%) after one week, underscoring its superior chemical durability. Remarkably, Ag–PCN demonstrated that enhanced faradaic efficiency (FE) post oxidative stress, likely due to structural and chemical rearrangements occurring during the stability test. In H-type cell experiments, Ag–PCN-7 achieved an H_2O_2 concentration of 1.55 mg L^{-1} within 2 hours, yielding a FE of 20% at 0.42 V *vs.* RHE. Additionally, Ag–PCN exhibited improved thermal stability compared to PCN. Density functional theory (DFT) calculations on a model heptazine Ag(I) complex revealed that Ag(I) serves as an active site, facilitating OOH* intermediate binding and mediating charge transfer from the PCN framework to the adsorbed species. Overall, these results establish Ag–PCN as a promising catalyst with high selectivity, remarkable chemical and thermal stability, and strong potential for electrochemical H_2O_2 production.

Received 23rd July 2025
Accepted 4th February 2026

DOI: 10.1039/d5ta05965h

rsc.li/materials-a

Introduction

Hydrogen peroxide (H_2O_2) is a versatile and environmentally friendly chemical widely used in industries such as bleaching, chemical synthesis, wastewater treatment, and disinfection.[1,2] Its demand is projected to rise significantly, with global production expected to reach 1.2 million tons by 2027.[3,4] Despite its importance, current industrial H_2O_2 production relies heavily on the energy-intensive anthraquinone process.[4,5] This process, while effective, has substantial drawbacks, including the generation of toxic waste byproducts, high operational costs, and significant expenses associated with the storage and transportation of H_2O_2 due to its instability.[6,7] These limitations demand the urgent need for alternative, eco-friendly, and energy-efficient methods for H_2O_2 production.

In this context, the electrocatalytic 2-electron oxygen reduction reaction ($2e^-$ ORR) under ambient conditions has emerged as a promising and sustainable approach.[8,9] This process operates under mild conditions, eliminating the need for energy-intensive steps, and directly produces H_2O_2, avoiding the challenges associated with transportation.[10] However, achieving high selectivity and stability in $2e^-$ ORR remains a key challenge.[11] Noble metals and their alloys, such as Pt,[12] Pd,[13] Au,[14] Pt–Hg,[15] Au–Pd,[16] and Pd–Hg,[17] have shown high selectivity and catalytic activity for H_2O_2 production *via* the $2e^-$ pathway. Yet, their widespread use is hindered by high costs, limited availability, and concerns over sustainability.

To address these issues, carbon-based single-atom catalysts (SACs) have emerged as promising alternatives.[18,19] SACs combine the advantages of noble metals, such as high catalytic activity, with the cost-effectiveness, abundance, and tunability of carbon-based materials.[20–22] Among these, polymeric carbon

[a]*Department of Chemistry, Bar-Ilan University, Ramat-Gan 5290002, Israel. E-mail: David.Zitoun@biu.ac.il*

[b]*Bar-Ilan Nanotechnology and Advanced Materials Institute, Bar-Ilan University, Ramat-Gan 5290002, Israel*

[c]*Materials Theory for Energy Scavenging (MATES) Lab, Department of Physics, Harish-Chandra Research Institute (HRI) Allahabad, A C.I. of Homi Bhabha National Institute (HBNI), Chhatnag Road, Jhunsi, Prayagraj (Allahabad) 211019, India*

† Equal contribution.

nitride (PCN) has garnered attention due to its unique electronic structure, tunable active sites, and straightforward synthesis.[23] Additionally, PCN's structural versatility allows for the incorporation of various single-atom metal sites, enabling precise modulation of its catalytic properties.[24] However, practical applications of PCN in the ORR for H_2O_2 production are hindered by its poor chemical stability under oxidative conditions, which limits its long-term durability.[25]

To overcome these challenges, we developed a highly selective and stable silver single-atom electrocatalyst incorporated into polymeric carbon nitride (Ag–PCN) using a supramolecular synthesis method. The resulting catalyst demonstrates excellent performance in the $2e^-$ ORR pathway, achieving H_2O_2 selectivity of approximately 86.22% in 0.1 M $KHCO_3$ and ~76.50% in 0.1 M KOH. For the first time, we report the Ag SA sites stabilize the PCN framework under H_2O_2-conditions. Chemical stability tests in 3% H_2O_2 reveal that after one week, PCN undergoes 9% mass loss, whereas Ag–PCN shows only ~1% mass loss, and ICP analysis indicates only 0.3 wt% decrease in Ag content, confirming both the enhanced structural robustness of Ag–PCN and the strong anchoring of Ag SAs. Consistently, Ag–PCN exhibits higher thermal stability than PCN, indicating that Ag improves the stability of the PCN support by providing strong N/C coordination sites. This interaction enhances O_2 adsorption and stabilizes the O–O bond, favoring selective H_2O_2 generation *via* the $2e^-$ ORR pathway. Interestingly, while pristine PCN initially shows higher H_2O_2 selectivity than Ag–PCN, the strong oxidative treatment induces surface reconstruction leading to pronounced increase in H_2O_2 selectivity for Ag–PCN that surpasses PCN under identical conditions in 0.1 M $KHCO_3$. In an H-type electrolytic cell, Ag–PCN achieves a H_2O_2 concentration of 1.55 mg L^{-1} within 2 h at 0.42 V *vs.* RHE, with a faradaic efficiency as high as 20%. After the chemical stability treatment, Ag–PCN delivers a markedly higher H_2O_2 yield and faradaic efficiency than the other catalysts tested, underscoring the beneficial effect of the oxidative conditioning and highlighting its superior catalytic performance and robustness relative to benchmark materials. Furthermore, PCN promotes water activation and facilitates HOO* intermediate formation. The interfacial water network enables efficient proton transfer, accelerating H_2O_2 production. Charge density analysis further indicates electron transfer from PCN to the *OOH intermediate adsorbed on Ag, underscoring the catalytic role of Ag–PCN in H_2O_2 synthesis. Overall, these results highlight that ultra-low-loading (~2.98 μg_{Ag} cm^{-2}) Ag SAs can significantly enhance electrochemical performance and stability, while simultaneously minimizing noble-metal usage, cost and resource consumption.

Results and discussion

The Ag–PCN catalyst was synthesized by thermal condensation of a supramolecular complex at 550 °C for 4 hours. The complete synthesis procedure provided in the SI. The formation of the self-assembled supramolecular phase and its morphology were confirmed by X-ray diffraction (XRD) and transmission electron microscopy (TEM), as shown in Fig. S1 and S2. The surface topography of Ag–PCN was further examined using high-resolution scanning electron microscopy (HR-SEM) and TEM (Fig. S3 and S4) which revealed the absence of Ag nanoparticles in the samples. Subsequently, high-angle annular dark-field scanning transmission electron microscopy (HAADF-STEM) imaging displayed distinct bright spots distributed over the sheet-like structure, indicating the presence of atomically dispersed Ag within the PCN framework (Fig. 1a, b and S5). Elemental mapping further verified the uniform distribution of Ag atoms throughout the PCN matrix (Fig. 1c–f). The Ag loading in the Ag–PCN sample was determined to be 4 wt% by inductively coupled plasma mass spectrometry (ICP-MS).

Powder X-ray diffraction (XRD) and X-ray photoelectron spectroscopy (XPS) were performed to study the structural and chemical properties of PCN and Ag–PCN. As shown in Fig. 2a, both PCN, Ag–PCN exhibit characteristic diffraction peaks at 13.0° and 27.2°, corresponding to the in-plane structural packing (100) and interlayer stacking (002) of heptazine units, respectively.[26–28] Notably, no additional peaks associated with Ag nanoparticles or Ag containing polymorphs were observed, confirming the atomic dispersion of Ag within the PCN matrix. The XPS survey spectra (Fig. 2b) revealed the presence of C, N, and O in both samples, while the additional Ag signals in Ag–PCN confirm the successful incorporation of Ag into the PCN framework. High-resolution Ag 3d spectra of Ag–PCN (Fig. 2c) display two distinct peaks at 374.29 eV (Ag $3d_{3/2}$) and 368.27 eV (Ag $3d_{5/2}$), with the spin–orbit splitting of 6.02 eV, characteristic

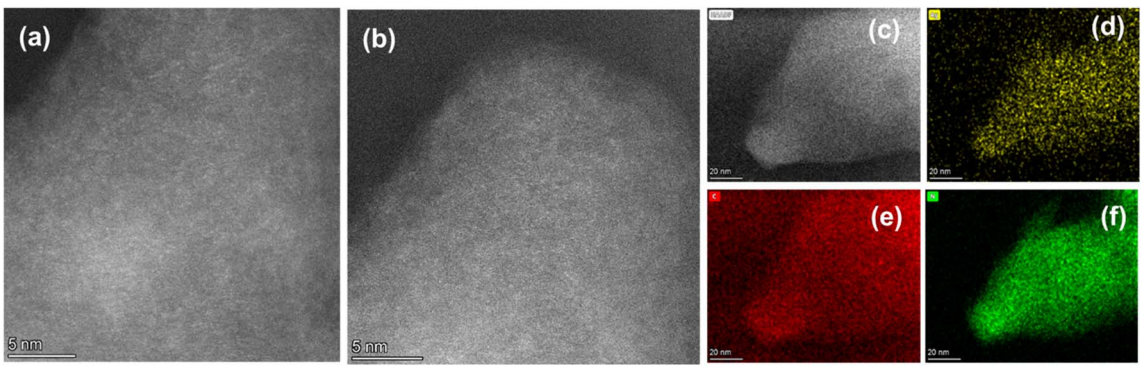

Fig. 1 (a and b) HAADF-STEM image, (c–f) corresponding elemental mapping of Ag–PCN SACs.

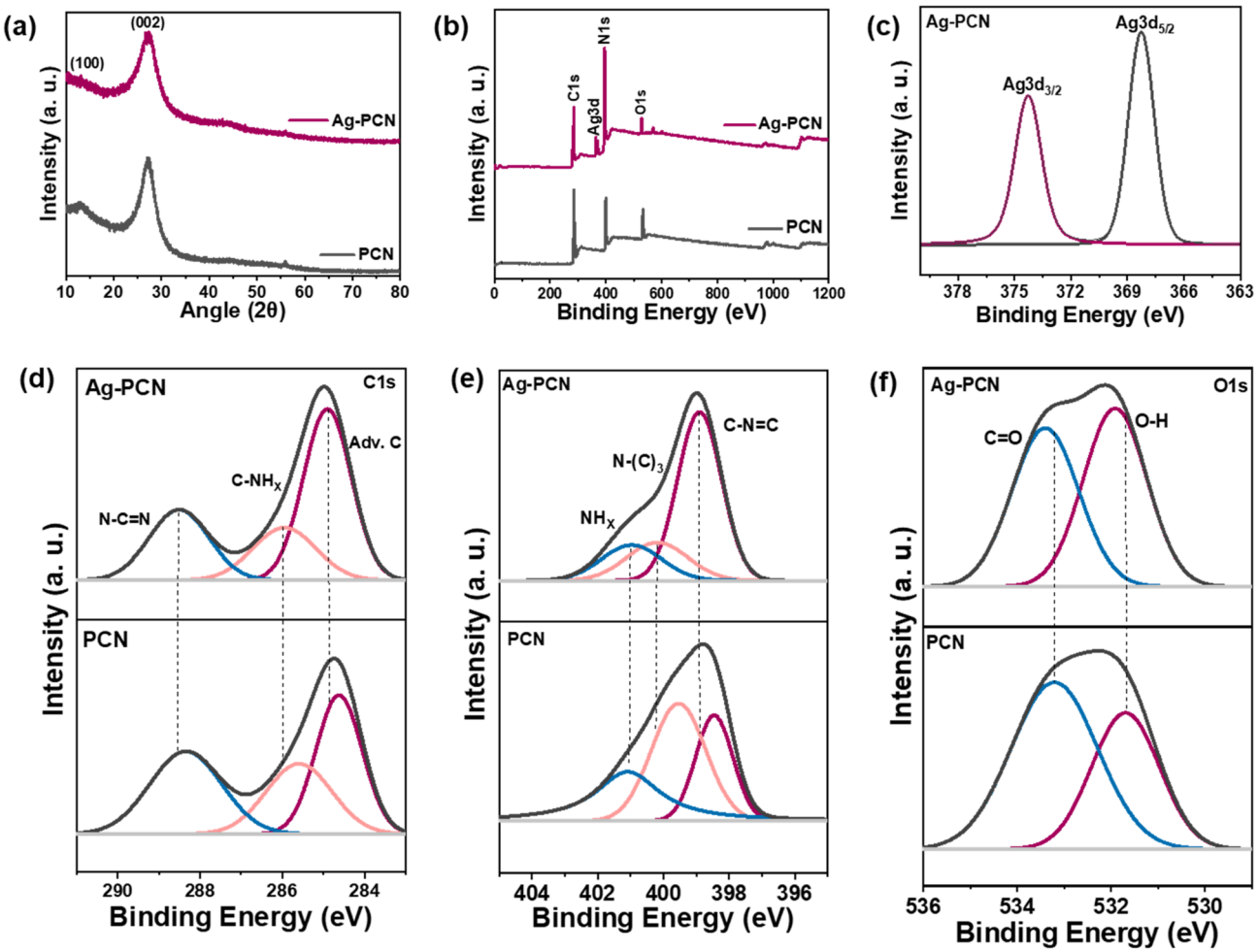

Fig. 2 (a) XRD pattern of PCN and Ag–PCN, (b) XPS survey spectra of PCN and Ag–PCN, (c–f) high resolution XPS spectra of, (c) Ag 3d in Ag–PCN, (d) C 1s, (e) N 1s, and (f) O 1s in PCN and Ag–PCN.

of metallic Ag.[29,30] The high-resolution C 1s spectra (Fig. 2d) of both PCN and Ag–PCN deconvoluted into three components at 284.60, 285.50, and 288.30 eV, corresponding to graphitic carbon (C–C/C=C), amino functionalities (C–NH_x, $x = 1, 2$) and the aromatic C=N bonds in the heptazine rings, respectively.[31] In Ag–PCN, a positive shift in binding energy was observed, suggesting electron withdrawal from carbon atoms due to Ag–N coordination, which reduces the electron density around carbon atoms. Similarly, N 1s spectra (Fig. 2e) were deconvoluted to three peaks at 398.82, 400.22, and 401.10 eV corresponding to C–N=C, N–$(C)_3$, and NH_x ($x = 1, 2$) respectively.[31,32] Apparently, the positive binding energy shift was observed in all three peaks, displaying that the encapsulation of single atom promotes the electron transfer from PCN to Ag. While the O 1s signal consists of two peaks at 531.91 and 533.40 eV due to C–O bond and surface adsorb water (Fig. 2f).[32]

Electrochemical ORR to produce H_2O_2 of PCN and Ag–PCN

To evaluate the electrocatalytic intrinsic activity and selectivity for $2e^-$ ORR was performed using rotating ring-disk electrode (RRDE) at 1600 rpm with three electrode configurations employed in an O_2 saturated 0.1 M $KHCO_3$ and 0.1 M KOH electrolyte. The ORR activity of all the prepared catalysts (PCN, Ag–PCN (12.5 mM, 25 mM and 37.5 mM)) was tested initially to identify the optimal Ag loading in PCN matrix for H_2O_2 production (Fig. S6). Among them PCN and Ag–PCN (25 mM) are chosen as suitable electrocatalysts for H_2O_2 activity and selectivity. The onset potential of PCN and Ag–PCN were approximately 0.7 V *vs.* RHE in 0.1 M KOH closely aligning with the theoretical equilibrium potential of $2e^-$ ORR (0.75 V *vs.* RHE). The highest current ring density of 0.6 mA cm^{-2} was obtained at 0.2 V *vs.* RHE, indicating its optimal $2e^-$ pathway tendency (Fig. 3a). The LSV curve of disk and ring current density in different rotation rates for PCN and Ag–PCN were shown in Fig. S7. Additionally, the PCN delivered 85.5% selectivity at 0.6 V and 77.8% at 0.2 V with corresponding electron transfer number (n) 2.28 and 2.44. Meanwhile, the H_2O_2 selectivity of Ag–PCN remains maintained at 77% (n 2.46) at 0.6 V and 75.8% selectivity (n 2.49) at 0.2 V respectively, which is the best among the other composites (Fig. 3b and c). Afterwards, catalytic stability of both PCN and Ag–PCN was analyzed by chronoamperometry measurement. As depicted in Fig. 3d–f, the Ag–PCN showed a small change in ring and disk current with maintained ~76.85% H_2O_2 selectivity for 18 h at 0.5 V *vs.* RHE

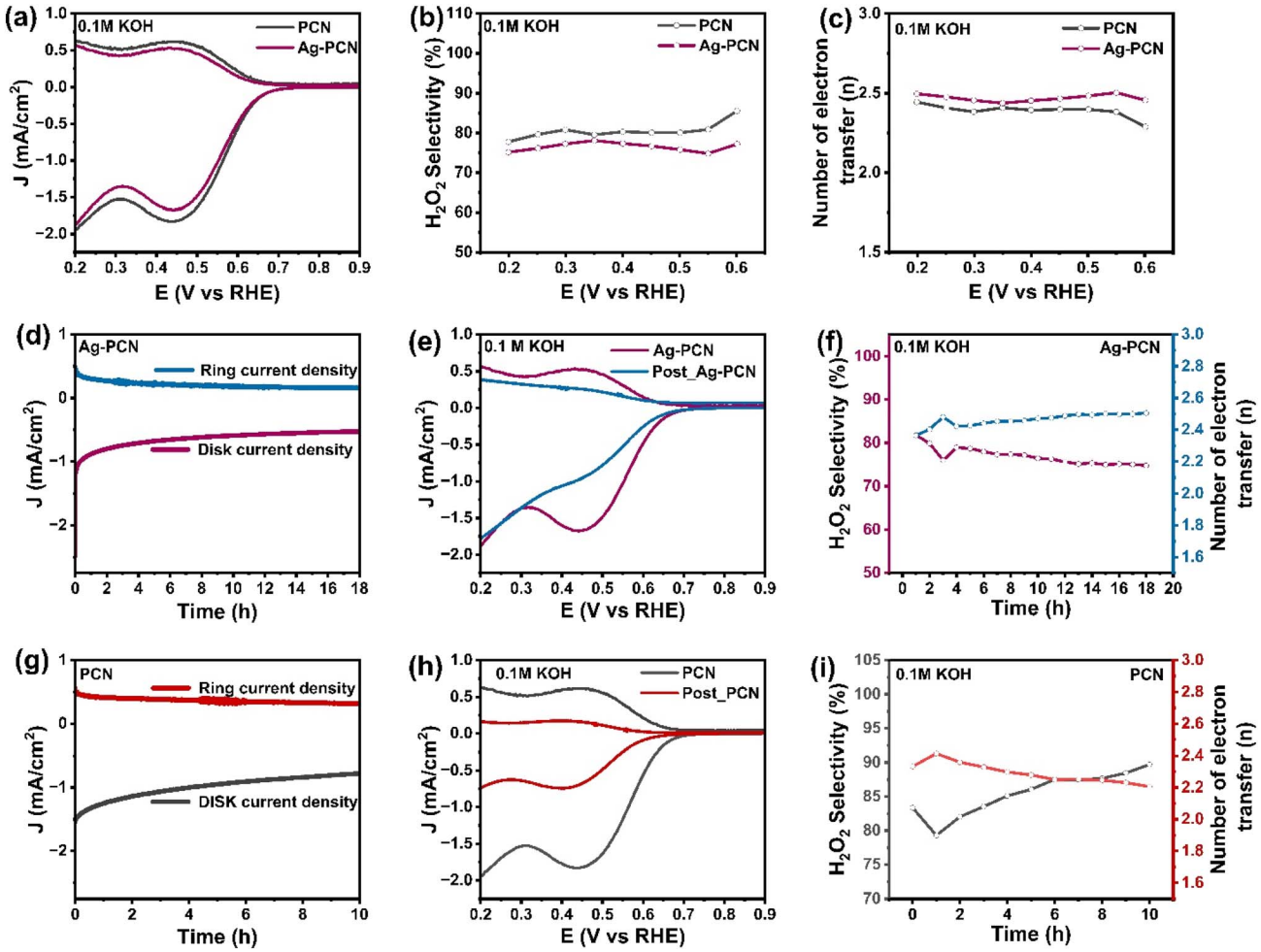

Fig. 3 H_2O_2 electroproduction in 0.1 M KOH. (a) LSV of PCN and Ag–PCN at 1600 rpm in O_2 saturated electrolyte, (b) H_2O_2 production selectivity of PCN and Ag–PCN, (c) number of electron transfer number (*n*) in PCN and Ag–PCN, (d) chronoamperometry measurement of Ag–PCN at 0.5 V *versus* RHE, (e) LSV of Ag–PCN after chronoamperometry test, (f) H_2O_2 selectivity and number of electron transfer with time in Ag–PCN, (g) chronoamperometry measurement of PCN at 0.5 V *versus* RHE, (h) LSV of PCN after chronoamperometry test, and (i) H_2O_2 selectivity and number of electron transfer with time in PCN.

with *n* of ~2.46, indicates the robust catalyst stability in alkaline media. However, the PCN indicates ~85.49% selectivity and with an *n* ~ 2.29 of 10 h at 0.5 V *vs.* RHE (Fig. 3g–i). Additionally, after durability test in the PCN deduced onset potential (0.65 V) and decrease in current density was observed. The low onset potential, directly related to the overpotential required to activate O_2, demonstrates that the Ag active site in Ag–PCN can effectively activate O_2 at low overpotential. Noticeably, the selectivity of PCN decreases to ~63.59%, while the electron transfer number increases to ~2.72 within the potential range of 0.20–0.60 V *vs.* RHE (Fig. S8a and b). In comparison, the selectivity of Ag–PCN reduces to around ~69.76%, with the electron transfer number increasing to ~2.60 within the same potential range (Fig. S8c and d). Faraday efficiency is very important for electrocatalysis, the initial FE is 74% for PCN at 0.6 V, whereas at 0.2 V FE decreases to 63%, in case of Ag–PCN, FE was 63% at 0.6 V and 60% at 0.2 V (Fig. S9). These results further underscore Ag–PCN's robustness and efficiency for oxygen reduction in alkaline media.

In addition to evaluating the best performance of PCN and Ag–PCN in alkaline media, their catalytic activity was also assessed in neutral electrolyte 0.1 M $KHCO_3$ under a rotation speed of 1600 rpm. Both catalysts exhibited a similar onset potential (~0.45 V *vs.* RHE) (Fig. 4a–c), which is characteristic of a thermodynamically favorable $2e^-$ ORR pathway under neutral pH. Over the potential range of 0 to 0.35 V *vs.* RHE, PCN exhibited H_2O_2 selectivity of 90.03% (*n* 2.19) at 0.35 V and 88.73% (*n* 2.22) at 0 V, indicating a dominant $2e^-$ oxygen reduction pathway. In comparison, Ag–PCN showed higher H_2O_2 selectivity of 93.58% (*n* 2.12) at 0.35 V and 82.07% (*n* 2.12) at 0.2 V, consistent with trends observed under alkaline conditions. Furthermore, FE were calculated in 0.1 M $KHCO_3$, PCN delivered an FE of 81.87% at 0.35 V and 79.74% at 0 V, while Ag–PCN achieved an FE of 87.95% at 0.35 V and 69.59% at 0 V (Fig. S10), further supporting the superior performance of Ag–PCN toward selective H_2O_2 generation. The rotation dependent LSV curve of both catalysts (Fig. S11a and b), further support the stable mass-transport controlled H_2O_2 generation in neutral media. The long-term stability of the

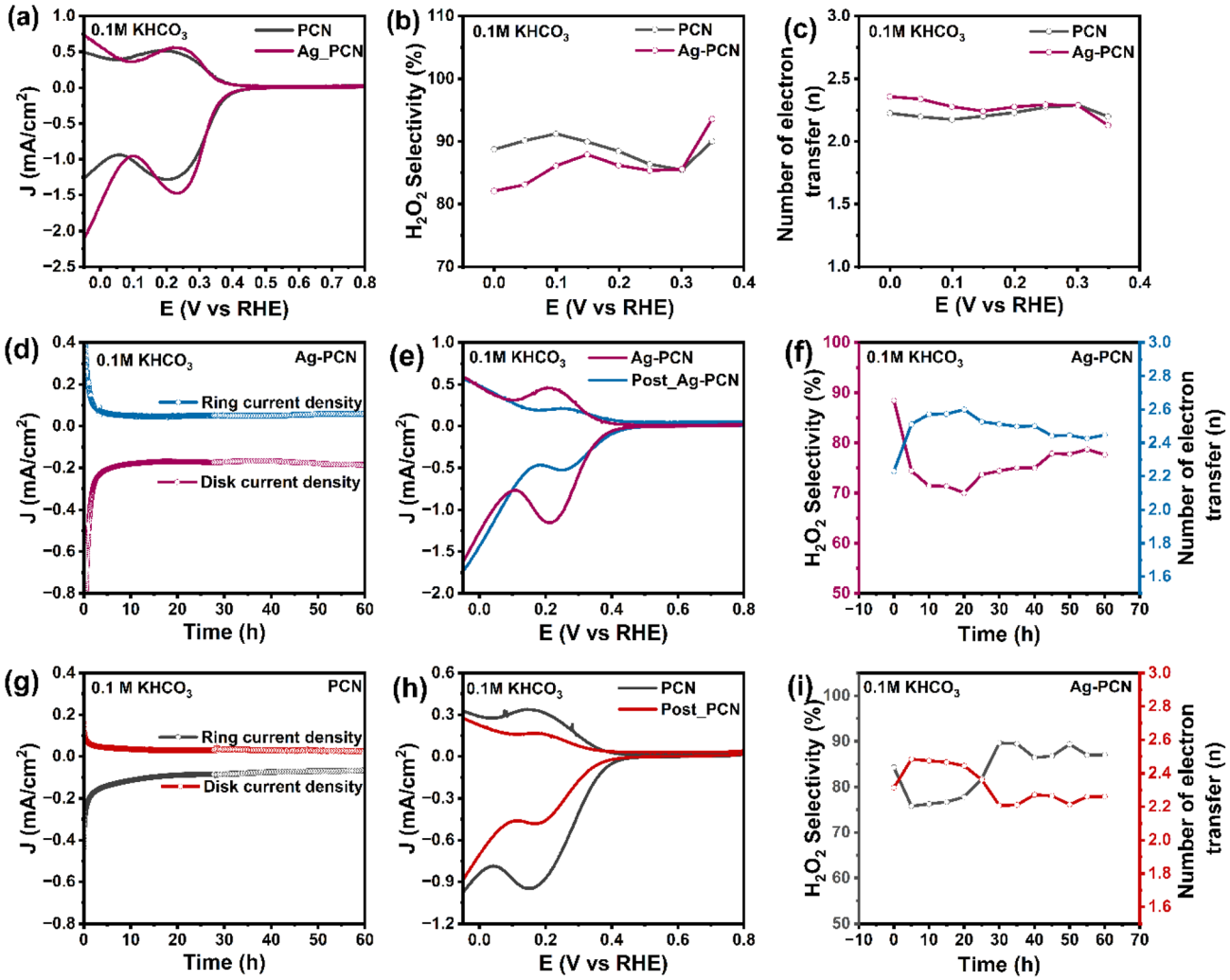

Fig. 4 H_2O_2 electroproduction in 0.1 M $KHCO_3$. (a) LSV of PCN and Ag–PCN at 1600 rpm in O_2 saturated electrolyte, (b) H_2O_2 production selectivity of PCN and Ag–PCN, (c) number of electron transfer number (*n*) in PCN and Ag–PCN, (d) chronoamperometry measurement of Ag–PCN at 0.2 V *versus* RHE, (e) LSV of Ag–PCN after chronoamperometry test, (f) H_2O_2 selectivity and number of electron transfer with time in Ag–PCN, (g) chronoamperometry measurement of PCN at 0.2 V *versus* RHE, (h) LSV of PCN after chronoamperometry test, and (i) H_2O_2 selectivity and number of electron transfer with time in PCN.

catalysts was assessed *via* chronoamperometric measurements at 0.2 V *vs.* RHE. Ag–PCN exhibited remarkable electrochemical durability, maintaining a H_2O_2 selectivity ranging from 70–75% with an average electron transfer number 2.48 over 60 hours of continuous operation (Fig. 4d–f). PCN, in contrast, maintained a slightly higher H_2O_2 selectivity ranging from ~78–83.71% and an *n* value of ~2.32 over the same duration (Fig. 4g–i). Notably, LSV measurements post-stability testing revealed a more positive onset potential for Ag–PCN, indicating a reduction in overpotential requirements likely attributed to surface restructuring, activation or stabilization of Ag active sites during extended electrolysis. To gain deeper understanding RRDE measurements were carried out after stability test (Fig. S12). PCN exhibits a slight reduction in H_2O_2 selectivity to 84.4% with an increased *n* value of 2.26, possibly due to catalyst degradation or structural rearrangement. In contrast, Ag–PCN showed improved selectivity of 88.35% and a lower electron transfer number (2.23), reaffirming the superior stability and robustness of Ag sites in promoting the selective $2e^-$ ORR even after prolonged operation. The calculated Faraday efficiency for PCN was 79% at 0 V and Ag–PCN was 69.8% whereas at 0.35 V, PCN was 82% and Ag–PCN demonstrated the highest Faraday efficiency of 87% (Fig. S10). Additionally, the LSV data for PCN and Ag–PCN in 0.1 M $KHCO_3$ and 0.1 M KOH, including error bars representing standard deviation from repeated measurements, are provided in the SI (see Fig. S21). This addition supports the reproducibility and reliability of our electrochemical measurements.

To assess the chemical stability of Ag–PCN and PCN under oxidative environment, 50 mg of each catalyst was immersed in 10 mL of 3% H_2O_2 for one week. Post treatment weight analysis (Table S1) revealed a 9% weight loss for PCN, indicating significant degradation, whereas, Ag–PCN exhibited only a 1% weight loss, confirming its superior stability. The enhanced oxidative resistance of Ag–PCN is attributed to the formation of Ag–N coordination bonds, which effectively passivate the reactive sites within the heptazine framework, and mitigate oxidative attack.

Consistently, ICP analysis shows that only 0.3 wt% Ag is lost during the one-week oxidative treatment, further demonstrating that Ag is strongly coordinated within the PCN matrix.

Post-stability high-angle annular dark-field scanning transmission electron microscopy (HAADF-STEM) was conducted to evaluate potential morphological evolution of the Ag/PCN catalyst. After one week of treatment, the support morphology and dispersion of Ag species remained unchanged, and no nanoparticle growth or agglomeration was detected. HAADF-STEM imaging combined with elemental mapping demonstrates that Ag is still present as isolated atomic sites homogeneously distributed on the PCN framework, indicating strong coordination between Ag centers and the PCN matrix (Fig. 5a–f). To further probe structural changes XRD pattern were recorded before and after H_2O_2 exposure. Ag–PCN-7 (post-H_2O_2 treated Ag–PCN) retained its characteristic peak at 27.3 (Fig. S13), indicating no change in the crystal structure. In contrast, PCN-7 (post H_2O_2 treated PCN), exhibited a slight peak shift to higher angle (27.4°), suggesting lattice contraction possibly induced oxidative degradation. These observations imply that Ag incorporation stabilizes the PCN framework under harsh oxidative conditions.

XPS analysis provided additional insights into surface composition and electronic environment. XPS survey spectra showed the signals of C, N, O and Ag for Ag–PCN-7 and C, N, and O signals for PCN (Fig. S14). Importantly, Ag–PCN displayed a slight negative binding energy shift in both C 1s and N 1s spectra after H_2O_2 exposure (Fig. 6a–c and S15) indicative of electron donation from Ag to the PCN framework. This electron transfer is believed to stabilize the structure by increasing the electron density around nitrogen and carbon atoms, reducing their susceptibility to oxidation. In contrast, PCN exhibited a positive shift in binding energy after H_2O_2 treatment (Fig. S16 and S17), suggesting the formation of oxidized functional groups and framework deterioration. Collectively, these results underscore the role of Ag–N coordination in enhancing the chemical stability of the material under harsh oxidative environment.

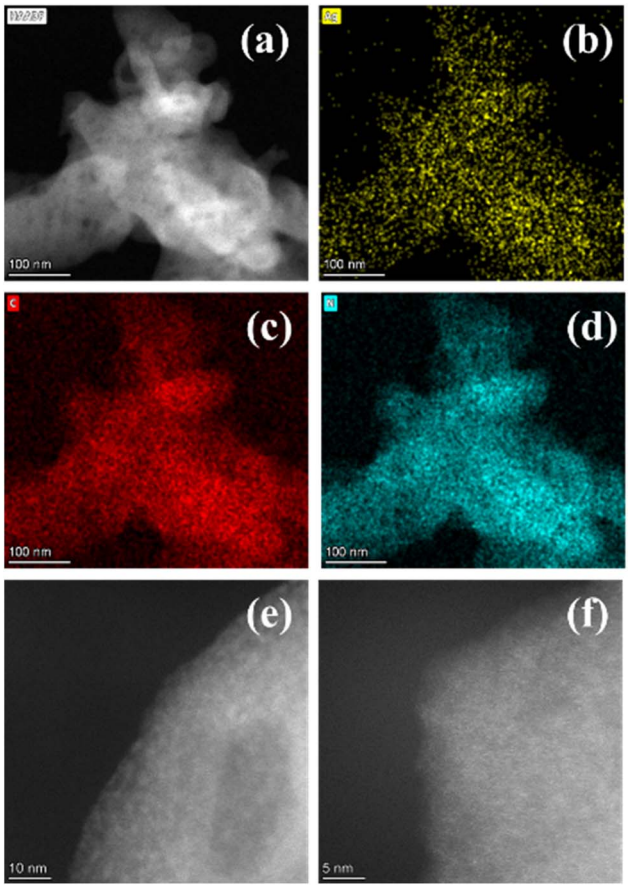

Fig. 5 HAADF-STEM analysis of Ag–PCN-7. (a–d) HAADF-STEM image and corresponding elemental mapping of Ag, C, and N. (e and f) HAADF-STEM images.

To further understand the chemical stability, Brunauer–Emmett–Teller (BET) surface area analysis was performed (Fig. 6d). The specific surface area increased from 52 $m^2\ g^{-1}$ for PCN to 93 $m^2\ g^{-1}$ for Ag–PCN. The higher surface area in Ag–PCN provides more accessible active sites for oxidative interaction, allowing better accommodation of oxidative stress and reducing localized degradation. The electronic changes after Ag encapsulated were also examined using solid-state ^{13}C CP-MAS NMR spectroscopy techniques (Fig. 6e). PCN displayed resonance at 164.56 ppm and 156.98 ppm assigned to C=N bonds and C=O defect sites in heptazine units, and a peak at 100.26 ppm, corresponding to the triazine rings. In Ag–PCN, these peaks shift to 164.18 ppm (upfield) and 157.8 ppm (downfield), 99.04 ppm, respectively. The upfield shift of the 164 ppm peak indicates increased electron density around C=N bonds due to Ag to nitrogen electron donation. The downfield shift of the 157 ppm peak suggests localized electron withdrawal, consistent with Ag–N bond formation. These observations confirm that Ag incorporation alters the electronic structure of PCN, enhancing chemical robustness. ^1H NMR spectra further supported these findings, with Ag–PCN showing deshielded peaks at (Fig. S18), indicating proton environments influenced by electronic redistribution caused by Ag coordination. The de-shielding effect highlights Ag's role in modulating local electronic environment, contributing to the framework's resistance to oxidative degradation.

Thermogravimetric analysis (TGA) from 30 °C to 800 °C in air revealed that both PCN and Ag–PCN undergo major decomposition between 300 °C and 600 °C (Fig. 6f), corresponding to decomposition of the polymeric carbon nitride framework. However, Ag–PCN exhibited a slower weight loss rate, and retained 10.7% of its weight at 800 °C, compared to only 4.5% for PCN. This enhanced thermal stability further supports that Ag incorporation reinforces the structural integrity of the matrix, likely through the formation of Ag–N interactions that stabilizes the carbon nitride framework.

Post-stability evaluation of electrocatalytic performance for H_2O_2 production

The electrocatalytic performance of PCN and Ag–PCN for the ORR toward H_2O_2 production was re-evaluated after 1 week of chemical stability testing in 3% H_2O_2. Measurements were performed both alkaline (0.1 M KOH) and neutral (0.1 M $KHCO_3$) electrolytes to assess the retention of catalytic

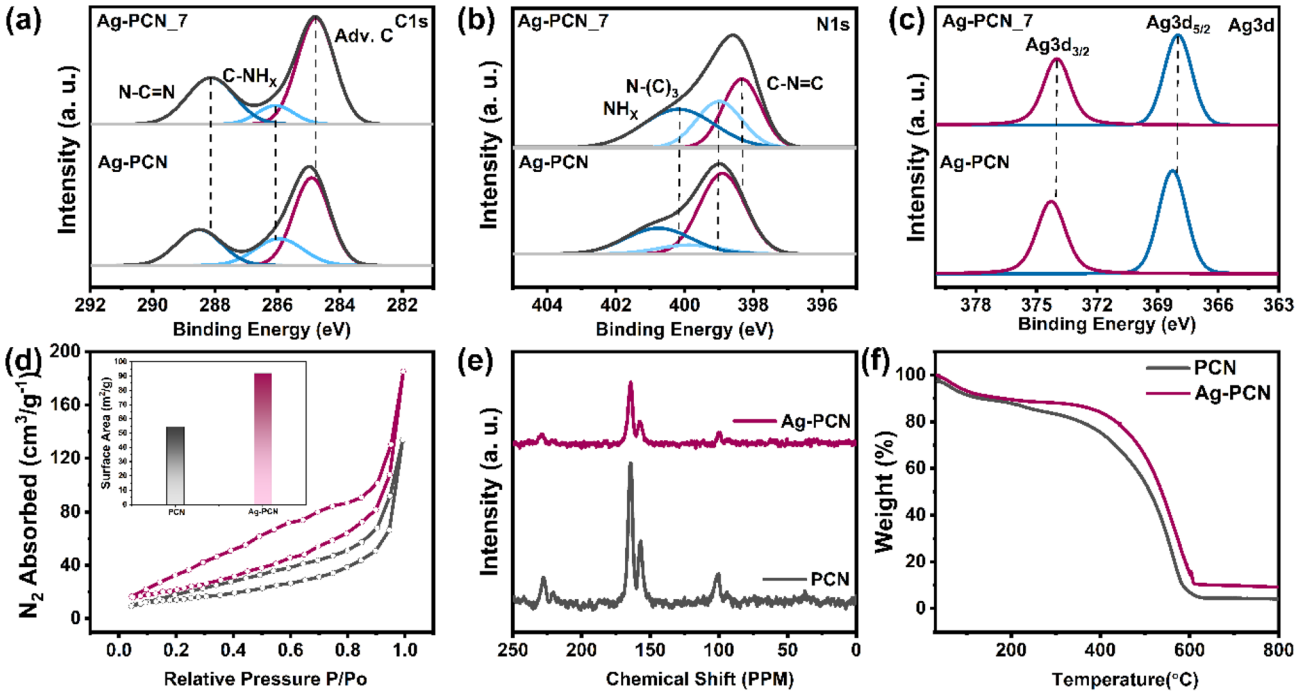

Fig. 6 High resolution XPS spectra of Ag–PCN before and after one week stability test in 3% H_2O_2 (a) C 1s in Ag–PCN and Ag–PCN_7, (b) N 1s in Ag–PCN and Ag–PCN_7, (c) Ag 3d in Ag–PCN and Ag–PCN_7, (d) nitrogen adsorption–desorption isotherm of PCN and Ag–PCN, (e) NMR spectra of PCN and Ag–PCN, and (f) TGA of PCN and Ag–PCN.

performance. In 0.1 M KOH, Ag–PCN_7 and PCN_7 exhibited H_2O_2 production selectivity of approximately 67.57% and 76.82%, respectively, with corresponding electron transfer numbers (n) of ~2.64 for Ag–PCN-7 and ~2.46 for PCN_7. Despite PCN-7 showing slightly higher selectivity, its LSV profile revealed more pronounced negative shifts in both ring and disk current density (Fig. 7a and b), indicating significant degradation. Conversely, Ag–PCN-7 exhibited only a slight negative shift in current density, demonstrating superior electrochemical stability and retention of catalytic activity (Fig. 7c and d). Although both materials retained comparable onset potentials, the stability–selectivity balance highlights Ag–PCN as more promising candidate for long-term electrocatalytic applications. In 0.1 M $KHCO_3$, Ag–PCN showed a slight positive shift in onset potential post chemical stability whereas PCN exhibited a slight negative shift (Fig. 7e–h). Both catalysts showed minimal changes in ring and disk current densities. Importantly, H_2O_2 selectivity increased to ~95.78% for Ag–PCN and ~94.15% for PCN, with the electron transfer numbers (n) remaining stable at ~2.11 and ~2.08, respectively, confirming the sustained $2e^-$ ORR activity in neutral media (Fig. S19). Structural and chemical modifications resulting from oxidative stress influenced the electrochemical behavior. In 0.1 M KOH, PCN showed a decrease in FE from 63.7–74% (0.2–0.6 V *vs.* RHE) to 59–65% after stress (Fig. S19a and d). In 0.1 M $KHCO_3$, PCN exhibited an increase from 79–82% (0–0.35 V *vs.* RHE) to 79–100% post-treatment (Fig. S19e and g). Similarly, Ag–PCN increased from 69–88% to 85–100% in the same potential range. These results highlight that while PCN maintains high H_2O_2 selectivity, its poor chemical stability significantly limits long-term usability. In contrast, Ag–PCN demonstrates a favorable balance of selectivity, faradaic efficiency, and durability, maintaining consistent performance under prolonged oxidative stress. A comparison with previously reported carbon nitride-based catalysts (Tables S2 and S3, SI) underscores the competitive performance of Ag–PCN among state-of-the-art systems. This improvement in H_2O_2 selectivity and faradaic efficiency after the chemical stability test may be attributed to changes occurring at the catalyst surface during the treatment. Exposure to 3% H_2O_2 under stability testing conditions likely facilitates the removal of residual impurities and initiates the formation or exposure of additional surface defects. Such processes can increase the number of accessible catalytic active sites and potentially modulate the local electronic environment, both of which are known to enhance selectivity and catalytic efficiency for the $2e^-$ oxygen reduction pathway.

To study the effect of single atom Ag in PCN for H_2O_2 synthesis, we performed density functional theory (DFT) based electronic structure computational calculations to model the two-electron catalytic reaction mechanism of H_2O_2 production. To model the catalytic mechanism, Ag single atom was coordinated at different sites (top of C, top of N atoms and inside the heptazine ring) available in the PCN 2D monolayer. The calculated formation energy was found to be widely negative (−0.89 eV) for Ag coordinated inside the heptazine ring of PCN sheet compared to the Ag coordination on top of C and N atoms. Large negative formation energy suggests that Ag coordination was thermodynamically favorable inside the PCN sheet (Fig. 8a), which is in good agreement with DFT studied literature on 3d transition metals embedded in PCN sheet.[33]

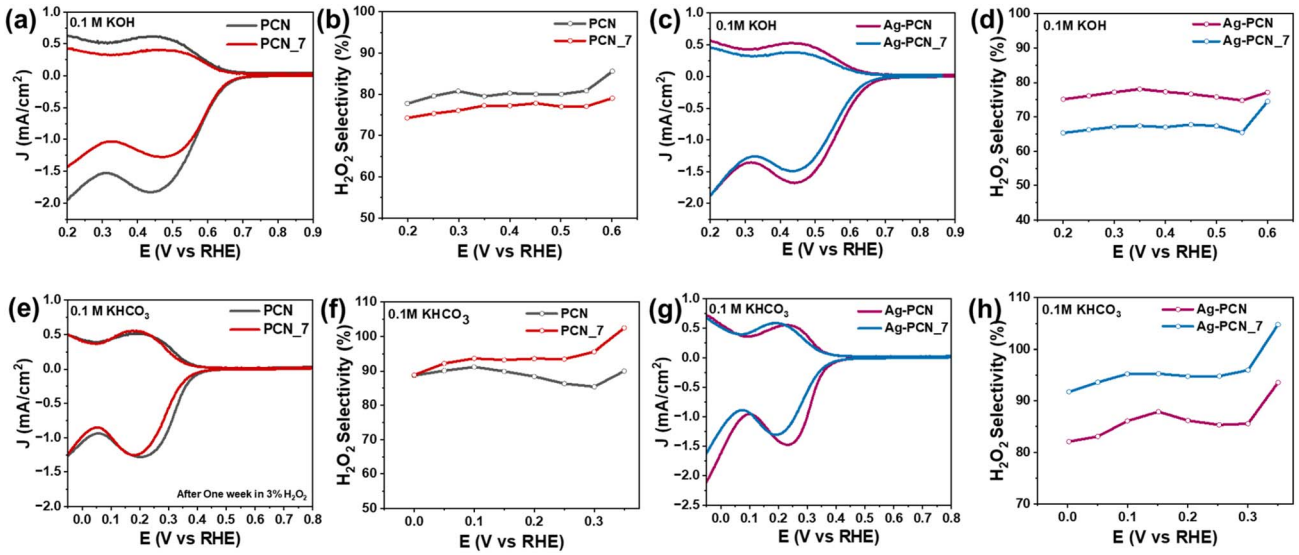

Fig. 7 H_2O_2 electroproduction in 0.1 M KOH and 0.1 M $KHCO_3$ after one-week chemical stability test in 3% H_2O_2 (a) LSV of PCN and PCN_7 (_7 meaning after one week), in 0.1 M KOH (b) H_2O_2 selectivity of PCN and PCN_7 in 0.1 M KOH, (c) LSV of Ag–PCN and Ag–PCN_7, in 0.1 M KOH (d) H_2O_2 selectivity of Ag–PCN and Ag–PCN_7 in 0.1 M KOH, (e) LSV of PCN and PCN_7, in 0.1 M $KHCO_3$ (f) H_2O_2 selectivity of PCN and PCN_7 in 0.1 M $KHCO_3$, (g) LSV of Ag–PCN and Ag–PCN_7, in 0.1 M $KHCO_3$ (h) H_2O_2 selectivity of PCN and PCN_7 in 0.1 M $KHCO_3$.

ORR occurs in two pathways, first is two-electron transfer pathway which produces H_2O_2 and second is four-electron transfer pathway which produces H_2O. In case of H_2O_2 production first O_2 adsorbs on surface which combines with proton couple electron gives *OOH intermediate which further combines with another proton couple electron transfer gives H_2O_2 production. The two-electron reaction pathway can be written as follows:

$$* + O_2 + (H^+ + e^-) = *OOH \quad (1)$$

$$*OOH + (H^+ + e^-) = H_2O_2 + * \quad (2)$$

Thus *OOH adsorption is main step for 2-electrocatalytic H_2O_2 production. It is well observed that when *OOH binding on catalyst surface should be moderate to enhance H_2O_2 production selectivity on catalyst surface. Therefore, *OOH adsorption energy was calculated to know the binding strength of *OOH on catalyst surface. Moreover, adsorption free energy of *OOH (which is a theoretical descriptor of reaction overpotential) with entropy (*TS*) and zero-point energy (ZPE) corrections were calculated. We calculated the *OOH adsorption free energy on C-atom inside Ag–PCN in the vicinity of Ag as well as *OOH adsorption energy on top of Ag single atom as shown in Fig. 8a and compared adsorption free energy of *OOH on top of C atom inside pristine PCN monolayer.

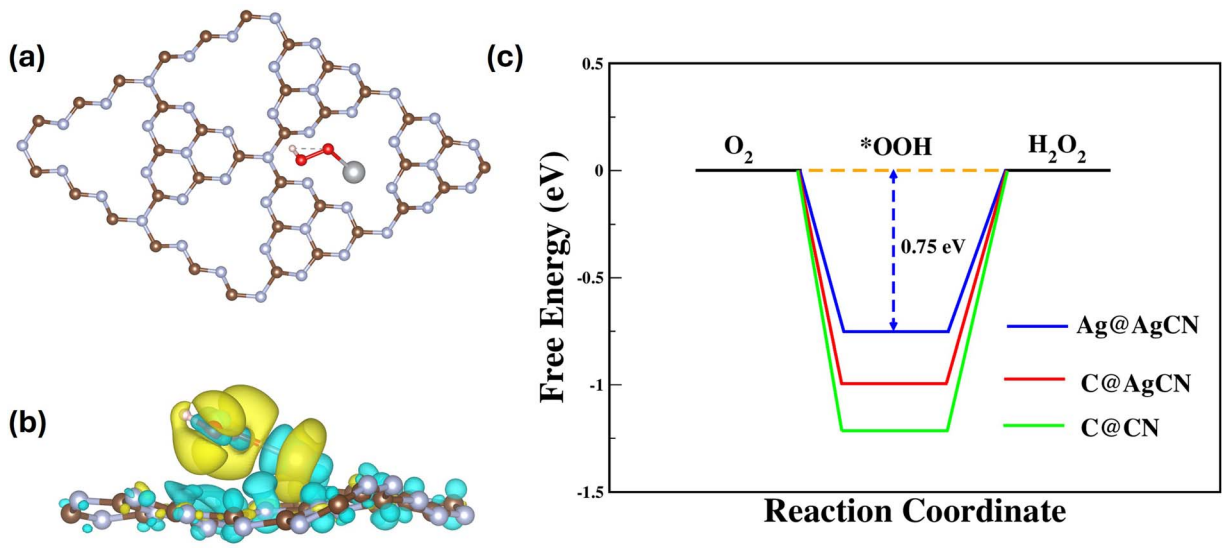

Fig. 8 (a) Crystal structure of polymeric carbon nitride sheet PCN monolayer (221 supercell structure) with *OOH adsorbed on Ag coordinated in the heptazine ring. (b) Charge density difference plot *OOH adsorbed on Ag. (c) Adsorption free energy profile of *OOH reaction intermediate at $U = 0.7$ V for three different adsorption sites on Ag–PCN.

Calculated adsorption free energies of *OOH at standard O_2 reduction potential ($U = 0.7$ V $\sim$ RHE) are given in Table S5. Adsorption free energy profile (ΔG_{*OOH}) demonstrates low overpotential (0.75 eV) for *OOH adsorption on top of Ag atom among all three considered cases (Table S5) as shown in Fig. 8c. Low overpotential of *OOH adsorption on top of Ag site confirms that Ag is an active catalytic site for H_2O_2 production inside Ag@PCN.

To study *OOH induced charged distribution and localization inside host PCN monolayer, charge density difference was calculated for both *OOH adsorbed on C atom in the vicinity of Ag atom and *OOH adsorbed on Ag atom. In the case of *OOH adsorbed on Ag atom; charge is getting accumulated (yellow color contour) on O atoms of *OOH as well as on Ag atom while charge depleted (cyan color contour) from PCN monolayer (Fig. 8b). Therefore, charge transfer from PCN monolayer to *OOH molecule will enhance catalytic H_2O_2 production activity on Ag supported PCN sheet. Further, electronic structure spin-polarized projected density of states (PDOS) calculations was performed to study the change in electronic structure after *OOH adsorption on different sites of C_3N_4 monolayer and Ag–C_3N_4 monolayer. Fig. S22a shows PDOS of pristine C_3N_4 monolayer which demonstrates valence band maxima (VBM) is created by N (p) orbitals while conduction band minima (CBM) are created by C (p) orbitals. Band gap value of pristine C_3N_4 monolayer from PDOS plot was found 1.18 eV (Table S6). In the case of *OOH adsorbed on top of Ag single atom PDOS contains O (p) and Ag (d) defect states in the band gap region which narrow down the band gap (0.32 eV) in comparison to pristine monolayer as shown in Fig. S22b and Table S6. Decrement in band gap will enhance conductivity and hence charge transfer resistance will decrease which will enhance the catalytic H_2O_2 production.

H_2O_2 electrosynthesis in H-cell

To systematically evaluate H_2O_2 production under practical device-like conditions, complementary to RRDE tests, H-type electrolytic cell experiments were performed. The experimental configuration (see Fig. S20a) employed a dual-compartment H-cell separated by a Nafion membrane, each side containing 45 mL of 0.1 M $KHCO_3$ electrolyte. Catalysts supported on carbon paper functioned as the working electrode accompanied by an Ag/AgCl reference electrode while a glassy carbon rod was used as the counter electrode in the opposite compartment. A continuous flow of O_2 was maintained throughout the working electrode chamber to ensure consistent reactant supply. Chronoamperometric measurements were conducted at a fixed potential for a duration of 2 hours. During electrolysis, aliquots (0.8 mL) of electrolyte were periodically sampled every 30 minutes from the working electrode compartment for subsequent quantification of H_2O_2 using UV-vis iodometry.

The chronoamperometric profiles (Fig. S20b) reveal that both PCN and Ag–PCN catalysts exhibit a gradual increase in current with time before reaching a steady state after extended operation. This behavior likely arises from progressive activation of surface or subsurface active sites, as small quantities of product generated during initial electrolysis may promote increased electrode wettability and facilitate enhanced ionic migration. In contrast, PCN-7 and Ag–PCN-7 show immediate current stability from the onset of measurements, indicating a high degree of accessible active sites and structural robustness under the applied operating conditions.

Quantitative H_2O_2 analysis, employing UV-vis iodometry (utilizing equimolar additions of potassium iodide and potassium hydrogen phthalate as colorimetric reagents and comparison with standard H_2O_2 solutions (Fig. S20c)), established that Ag–PCN-7 consistently outperformed other catalysts, the production rate of 0.93 mg L^{-1} at 30 minutes and 1.55 mg L^{-1} at 120 minutes. While Ag–PCN achieved nearly quantitative faradaic efficiency ($\sim$100%) during the initial phase of the experiment, a pronounced decline to 11% was observed after 120 minutes. Conversely, both PCN-7 and Ag–PCN-7 demonstrated strong retention of faradaic efficiency over extended operation, whereas PCN and Ag–PCN experienced significant losses (Fig. S20d).

These results distinctly highlight an inverse relationship between current density and faradaic efficiency across certain catalyst systems most notably in PCN and Ag–PCN. As current density increases over the course of the experiment, faradaic efficiency diminishes substantially. This phenomenon is attributed to an escalating prevalence of undesired side reactions, such as H_2O_2 reduction and decomposition, which are favored at higher currents and rising local product concentrations. Such effects underscore the critical interplay between maintaining high activity and preserving selectivity during device-scale H_2O_2 electrosynthesis, reaffirming the necessity for structural and compositional catalyst optimization to mitigate efficiency losses at elevated current densities. These findings are consistent with our observations from RRDE measurements. The production rate of H_2O_2 and faradaic efficiency of PCN, PCN-7, Ag–PCN, and Ag–PCN-7 were compared with recently reported SAs based catalysts (Table S4).

From a technoeconomic standpoint, previous assessments of electrochemical H_2O_2 production with GDEs have shown that electricity and other operating costs dominate the overall production cost, whereas electrode material contributes only a minor fraction.[34] Given the low-cost PCN support and ultra-low Ag loading in Ag–PCN, the catalyst material cost is expected to have negligible impact compared to energy consumption and cell design considerations.

Conclusion

In conclusion, we successfully developed Ag single-atom coordinated carbon nitride (Ag–PCN) framework that serves as an efficient and stable electrocatalyst for $2e^-$ ORR pathway to H_2O_2 with ultra-low-loading, even under highly oxidative conditions. The catalyst exhibited remarkable activity and selectivity for electrocatalytic H_2O_2 production in both alkaline and neutral media. Combined experimental and theoretical study demonstrates that the coordination of Ag single atoms in PCN is thermodynamically stable and brings more active catalytic site for the $2e^-$ ORR mechanism, reaching 93% H_2O_2 selectivity at 0.35 V *vs.* RHE 0.1 M $KHCO_3$. Ag coordination substantially enhances chemical stability of the PCN framework *via* Ag–N bonds formation, which governs oxidative degradation through charge transfer to the metal centers and thereby stabilizes the structure. Our experimental findings demonstrates that a nine-fold improvement in

durability during accelerated stress tests in 3% H_2O_2 for Ag–PCN compared to PCN, with a significant enhancement in H_2O_2 selectivity and faradaic efficiency, achieving 100% in 0.1 M $KHCO_3$ after post-stability treatment. In an H-type electrolytic cell, Ag–PCN-7 attains an H_2O_2 yield of 1.55 mg L^{-1} after 2 hours at 0.42 V *vs.* RHE, outperforming the other catalysts under identical conditions. The superior stability, selectivity, and production yield of Ag–PCN-7 underscore its significant potential for sustainable and efficient electrochemical H_2O_2 synthesis.

Conflicts of interest

There are no conflicts to declare.

Data availability

All the data presented in an article is available in the manuscript.

Supplementary information (SI) is available. See DOI: https://doi.org/10.1039/d5ta05965h.

Acknowledgements

D. Z. acknowledges partial funding from the Israel Science Foundation (grant 2023/1471) and S. K. S. and S. C. would like to acknowledge Harish-Chandra Research Institute (HRI) Allahabad for the infrastructure and funding. Computational work for this study was carried out at the cluster computing facility at HRI Allahabad (https://www.hri.res.in/cluster).

References

1 S. Yang, A. Verdaguer-Casadevall, L. Arnarson, L. Silvioli, V. Čolić, R. Frydendal, J. Rossmeisl, I. Chorkendorff and I. E. L. Stephens, *ACS Catal.*, 2018, **8**, 4064.
2 A. Huang, R. S. Delima, Y. Kim, E. W. Lees, F. G. L. Parlane, D. J. Dvorak, M. B. Rooney, R. P. Jansonius, A. G. Fink, Z. Zhang and C. P. Berlinguette, *J. Am. Chem. Soc.*, 2022, **144**, 14548.
3 Q. Ruan, *ChemCatChem*, 2024, **16**, e202301082.
4 W. Zhao, P. Yan, B. Li, M. Bahri, L. Liu, X. Zhou, R. Clowes, N. D. Browning, Y. Wu, J. W. Ward and A. I. Cooper, *J. Am. Chem. Soc.*, 2022, **144**, 9902.
5 M. Song, W. Liu, J. Zhang, C. Zhang, X. Huang and D. Wang, *Adv. Funct. Mater.*, 2023, **33**, 2212087.
6 S. Khan, M. A. Qaiser, W. A. Qureshi, S. N. uz Z. Haider, X. Yu, W. Wang and Q. Liu, *J. Environ. Chem. Eng.*, 2024, **12**, 114143.
7 J. M. Campos-Martin, G. Blanco-Brieva and J. L. G. Fierro, *Angew. Chem., Int. Ed.*, 2006, **45**, 6962.
8 N. Wang, S. Ma, P. Zuo, J. Duan and B. Hou, *Adv. Sci.*, 2021, **8**, 2100076.
9 X. Shi, S. Back, T. M. Gill, S. Siahrostami and X. Zheng, *Chem*, 2021, **7**, 38.
10 L. Zhao, R. Yan, B. Mao, R. Paul, W. Duan, L. Dai and C. Hu, *Small*, 2024, **20**, 2403029.
11 H. Yang, N. An, Z. Kang, P. W. Menezes and Z. Chen, *Adv. Mater.*, 2024, **36**, 2400140.
12 C. H. Choi, H. C. Kwon, S. Yook, H. Shin, H. Kim and M. Choi, *J. Phys. Chem. C*, 2014, **118**, 30063.
13 R. Liu, C. Wang, Y. Yan, R. Wang and G. Chen, *ACS Catal.*, 2024, **14**, 3955.
14 J. S. Jirkovský, M. Halasa and D. J. Schiffrin, *Phys. Chem. Chem. Phys.*, 2010, **12**, 8042.
15 S. Siahrostami, A. Verdaguer-Casadevall, M. Karamad, D. Deiana, P. Malacrida, B. Wickman, M. Escudero-Escribano, E. A. Paoli, R. Frydendal, T. W. Hansen, I. Chorkendorff, I. E. L. Stephens and J. Rossmeisl, *Nat. Mater.*, 2013, **12**, 1137.
16 J. S. Jirkovský, I. Panas, E. Ahlberg, M. Halasa, S. Romani and D. J. Schiffrin, *J. Am. Chem. Soc.*, 2011, **133**, 19432.
17 A. Verdaguer-Casadevall, D. Deiana, M. Karamad, S. Siahrostami, P. Malacrida, T. W. Hansen, J. Rossmeisl, I. Chorkendorff and I. E. L. Stephens, *Nano Lett.*, 2014, **14**, 1603.
18 L. Sun, X. Jin, T. Su, A. C. Fisher and X. Wang, *Adv. Mater.*, 2024, **36**, 2306336.
19 W. Liu, R. Chen, Z. Sang, Z. Li, J. Nie, L. Yin, F. Hou and J. Liang, *Adv. Mater.*, 2024, **36**, 2406403.
20 M. Shanmugasundaram, N. R. Samala, I. Grinberg and D. Zitoun, *ACS Catal.*, 2024, 13877.
21 X. Wang, R. Huang, X. Mao, T. Liu, P. Guo, H. Sun, Z. Mao, C. Han, Y. Zheng, A. Du, J. Liu, Y. Jia and L. Wang, *Adv. Sci.*, 2024, **11**, 2402240.
22 Y. Zhou, G. Gao, J. Kang, W. Chu and L. W. Wang, *Nanoscale*, 2019, **11**, 18169.
23 G. F. S. R. Rocha, M. A. R. da Silva, A. Rogolino, G. A. A. Diab, L. F. G. Noleto, M. Antonietti and I. F. Teixeira, *Chem. Soc. Rev.*, 2023, **52**, 4878.
24 S. Mehmood, S. Sk, B. M. Abraham, M. Ahmadipour, U. Pal and J. Dutta, *Adv. Funct. Mater.*, 2024, 2418602.
25 J. Xiao, Q. Han, Y. Xie, J. Yang, Q. Su, Y. Chen and H. Cao, *Environ. Sci. Technol.*, 2017, **51**, 13380.
26 H. Niu, W. Zhao, H. Lv, Y. Yang and Y. Cai, *Chem. Eng. J.*, 2021, **411**, 128400.
27 K. Eid, M. H. Sliem, M. Al-Ejji, A. M. Abdullah, M. Harfouche and R. S. Varma, *ACS Appl. Mater. Interfaces*, 2022, **14**, 40749–40760.
28 M. Chu, K. Hu, J. Wang, Y. Liu, S. Ali, C. Qin and L. Jing, *Appl. Catal., B*, 2019, **243**, 57.
29 C. Hu, J. Hu, Z. Zhu, Y. Lu, S. Chu, T. Ma, Y. Zhang and H. Huang, *Angew. Chem., Int. Ed.*, 2022, **61**, e202212397.
30 F. Wang, Y. Wang, Y. Feng, Y. Zeng, Z. Xie, Q. Zhang, Y. Su, P. Chen, Y. Liu, K. Yao, W. Lv and G. Liu, *Appl. Catal., B*, 2018, **221**, 510.
31 A. Gupta, T. Bhoyar, B. M. Abraham, D. J. Kim, K. S. Pasupuleti, S. S. Umare, D. Vidyasagar and A. Gedanken, *ACS Appl. Mater. Interfaces*, 2023, **15**, 18898.
32 T. Bhoyar, B. M. Abraham, A. Gupta, D. J. Kim, N. R. Manwar, K. S. Pasupuleti, D. Vidyasagar and S. S. Umare, *J. Mater. Chem. A*, 2024, **12**, 979.
33 D. Ghosh, G. Periyasamy and S. K. Pati, *J. Phys. Chem. C*, 2014, **118**, 15487.
34 E. Zhao, G. Xia, Y. Li, J. Zhan, G. Yu and Y. Wang, *ACS ES&T Eng.*, 2023, **3**, 1800.

